



Research
Environmental Engineering—Article

Simultaneous Denitrification and Decarbonization of Wastewater over *In Situ* Generation of $\cdot\text{ClO}$ Radicals Through a Fast, High-Performance Electro-Filtration Process



Bin Zhao^{a,b,#}, Jialin Yang^{a,c,#}, Ruiping Liu^b, Jiuhui Qu^{a,b}, Meng Sun^{a,b,*}

^a Key Laboratory of Environmental Aquatic Chemistry, State Key Laboratory of Regional Environment and Sustainability, Research Center for Eco-Environmental Sciences, Chinese Academy of Sciences, Beijing 100085, China

^b Center for Water and Ecology, State Key Joint Laboratory of Environment Simulation and Pollution Control, School of Environment, Tsinghua University, Beijing 100084, China

^c Science and Technology Innovation Center for Municipal Wastewater Treatment and Water Quality Protection, School of Environment, Northeast Normal University, Changchun 130117, China

ARTICLE INFO

Article history:

Received 3 November 2024

Revised 20 May 2025

Accepted 11 July 2025

Available online 16 July 2025

Keywords:

Wastewater treatment

Denitrification

Decarbonization

Chlorine oxide radical

Electro-reactive membranes

ABSTRACT

The contamination of wastewater with organic pollutants and nitrogen compounds poses significant environmental challenges. The primary objective of wastewater treatment is the simultaneous denitrification and decarbonization of ammonia nitrogen and organics into harmless by-products. This study presents a novel method for the directional generation of chlorine radical species like $\cdot\text{ClO}$ and $\cdot\text{Cl}$ using electro-reactive membranes (EMs) known as $\text{RuO}_2@\text{PbO}_2\text{-M}$, which were fabricated using an electro-deposition coupled template approach. This method facilitates the rapid and efficient conversion of ammonia to nitrogen and concurrently reduces the chemical oxygen demand in the effluent. Our system achieved ultra-efficient simultaneous denitrification and decarbonization with minimal energy consumption in single-filtration mode, thereby eliminating the need for chemical precursors. We elucidate the formation pathway of $\cdot\text{ClO}$ and $\cdot\text{Cl}$ during the electrochemical oxidation process involving $\text{RuO}_2@\text{PbO}_2\text{-M}$, where $\cdot\text{Cl}$ generated from RuO_2 reacts with $\cdot\text{OH}$ from PbO_2 under hypochlorous acid conditions, thereby enhancing nitrogen and carbon removal. These findings highlight a novel electro-filtration and an innovative reactive membrane design for $\cdot\text{ClO}$ synthesis, which provides a new research framework for the concurrent removal of nitrogen and carbon, and offers a promising solution to enhance wastewater treatment efficiency.

© 2025 THE AUTHORS. Published by Elsevier LTD on behalf of Chinese Academy of Engineering and Higher Education Press Limited Company. This is an open access article under the CC BY-NC-ND license (<http://creativecommons.org/licenses/by-nc-nd/4.0/>).

1. Introduction

Discharges of organic wastewater containing ammonia (NH_3) and dissolved organic matter (DOC) can cause the deterioration of water bodies [1–3], which results in water eutrophication and the death of aquatic organisms [4,5]. Traditional water-treatment methods for denitrification and decarbonization are commonly used in municipal wastewater treatment systems, however, they have limitations in carbon source supplementation and nitrogen removal efficiency [6–8]. Consequently, there is a compelling requirement to develop highly efficient and easy-to-operate

methods to achieve simultaneous denitrification and decarbonization of wastewater.

Electrochemical technologies are environmentally friendly and low-pollution water treatment methods [9,10]. The electrochemical oxidation of ammonia can be divided into direct and indirect processes [11]. During direct oxidation, ammonia adsorbed on the anode surface is converted to nitrogen (N_2) through electron transfer [12]. During indirect oxidation, reactive oxygen species (ROS) are produced on the electrode surface and the adsorbed ammonia is oxidized to nitrogen [13,14]. Moreover, chloride ions in the effluent can be oxidized to form reactive chlorine species (RCS), which enhance ammonia oxidation and accelerate nitrogen removal [15,16]. During the RCS synthesis process, various chlorine radicals and reactive species such as hypochlorous acid (HOCl), chlorine free radicals ($\cdot\text{Cl}$), and chlorine oxygen free radicals ($\cdot\text{ClO}$)

* Corresponding author.

E-mail address: mengsun@rcees.ac.cn (M. Sun).

These authors contributed equally to this manuscript.

are generated near the anode [17,18]. Because of the high redox potential of $\cdot\text{ClO}$, it reacts rapidly with electron-rich compounds [19,20], and its reaction rate with NH_3 is two to three orders of magnitude higher than that of hydroxyl radical ($\cdot\text{OH}$) and $\cdot\text{Cl}$, respectively [21]. In the region near the anode, $\cdot\text{ClO}$ is usually produced during the scavenging of $\cdot\text{OH}$ by HClO or free chlorine (ClO^-) [18,22]. Therefore, controlling the conversion of $\cdot\text{OH}$ and $\cdot\text{Cl}$ to $\cdot\text{ClO}$ by regulating the active sites of the catalyst is crucial for achieving efficient denitrification.

Furthermore, although extensive research has been performed on the application of electrochemical ammonia oxidation (EAOR) technology for ammonia-nitrogen removal in water treatment, challenges remain in extending its use to the entire wastewater treatment industry [23]. The lifespan of the free radicals formed on the electrode surface is short, and is limited to a thin layer less than 1 μm from the anode surface [24]. Therefore, it is essential to design advanced low-pollution surfaces to ensure high reaction kinetics, particularly for the specific *in situ* generation of the target radical $\cdot\text{ClO}$ [25]. Augmentation of electrocatalytic potency necessitates chemical reagent circumvention, which concomitantly truncates hydraulic retention duration, mitigates intra-reactor transport constraints, and elevates Faradaic yield coefficients within the electron-transfer regime [26]. Incorporating catalysts into highly electro-reactive membranes (EMs) used in flow-through operations could potentially address the challenges related to limited reaction rates and N_2 selectivity when treating NH_3 -laden wastewater [27]. Porous membranes have proven to be ideal electrode substrates for enhancing the electrocatalytic performance [28,29]. Continuous flow through EMs with high electrode surface areas can enhance mass transport and maximize the catalyst utilization efficiency [30]. These porous substrates spatially confine the reactants and electrify the active sites at the micrometer and nanometer scales. The efficiency of the spatial generation of $\cdot\text{ClO}$ can also be improved owing to the spatial confinement of the membrane pores and channels, which facilitates faster rates of *in situ* radical generation within the membrane pores [31]. Considering their dual selectivity and solute separation functionality, EMs can be easily integrated into existing systems, such as electrochemical oxidation systems and capacitive deionization (CDI), or used as on-the-spot devices for water treatment [15,32]. However, few examples of EMs for simultaneous denitrification and decarbonization of wastewater have been successfully introduced.

In this study, an electrocatalytic membrane for ultraefficient $\cdot\text{ClO}$ production is proposed. The electro-reactive membrane ($\text{RuO}_2@\text{PbO}_2\text{-M}$) features electrochemically reactive surfaces formed by reverse electrodeposition of β -lead dioxide ($\beta\text{-PbO}_2$) and coating the ruthenium dioxide (RuO_2) supports. The efficacy of *in situ* generated $\cdot\text{ClO}$ is evaluated for simultaneous denitrification and decarbonization during elector-filtration using acetaminophen (APAP) as a simulated contaminant. The rapid conversion mechanism of EAOR is further investigated. The co-existence of $\cdot\text{ClO}$ and its precursors was confirmed, and their spatiotemporal distribution was investigated throughout the $\text{RuO}_2@\text{PbO}_2\text{-M}$ during the electro-filtration. The treatment mechanism of $\text{RuO}_2@\text{PbO}_2\text{-M}$ was investigated for the efficient purification of organic wastewater containing NH_3 using an electro-filtration system. This study provides a new research approach for the catalytic oxidation of an electrode to treat organic ammonia wastewater.

2. Material and methods

2.1. Materials

Analytical-grade sodium sulfate (Na_2SO_4), ammonium sulfate ($(\text{NH}_4)_2\text{SO}_4$), sodium chloride (NaCl), sodium fluoride (NaF), lead

nitrate ($\text{Pb}(\text{NO}_3)_2$), nitric acid (HNO_3), and ruthenium(III) chloride (RuCl_3) were purchased from Sinopharm Chemical Reagent Co., Ltd., China. Nitrobenzene (NB), tert-butanol (TBA), and sodium bicarbonate (NaHCO_3) were purchased from Aladdin Industrial Corporation (China). All the solutions were prepared using deionized water.

2.2. Preparation of the $\text{RuO}_2@\text{PbO}_2\text{-M}$

Commercial 300 mesh titanium powder (purity > 99.5%) was evenly distributed in a crucible and placed in a vacuum drying oven at 60 $^\circ\text{C}$ for 2 h. After drying, the titanium (Ti) powder was weighed and spread in a mold with a diameter of 47 mm, at a pressing pressure of 35 bar (1 bar = 10^5 Pa) for a pressing time of 15 min. It was then calcined at high temperature (550 $^\circ\text{C}$) for 2 h under an inert argon atmosphere to obtain Ti-membrane (M). The Ti-M was placed in an acidic solution (0.1 $\text{mol}\cdot\text{L}^{-1}$ HNO_3 , 0.5 $\text{mol}\cdot\text{L}^{-1}$ $\text{Pb}(\text{NO}_3)_2$, and 0.04 $\text{mol}\cdot\text{L}^{-1}$ NaF). A layer of $\beta\text{-PbO}_2$ was electrodeposited on the surface of Ti-M by applying a current density of 60 $\text{mA}\cdot\text{cm}^{-2}$ for 20 min, followed by 30 $\text{mA}\cdot\text{cm}^{-2}$ for 40 min, the product was named lead dioxide membrane ($\text{PbO}_2\text{-M}$). Span 80 and Tween 80 were mixed in a mass ratio of 8:2, and organic supports with a carbon framework were prepared through pyrolysis under nitrogen protection. The RuCl_3 gel was mixed with the organic supports and coated onto $\text{PbO}_2\text{-M}$ using a brushing method, and the carbon framework was removed by high-temperature (muffle furnace calcination, hold 1 h) calcination to produce the final membrane, $\text{RuO}_2@\text{PbO}_2\text{-M}$.

2.3. Analytical methods

The phase and crystallinity were measured using X-ray diffraction (XRD; D/max 200 PC, Rigaku, Japan). The morphologies of the prepared electrodes were characterized by scanning electron microscopy (SEM; Hitachi SU8010, Hitachi, Japan) and energy-dispersive X-ray spectroscopy (EDS; Hitachi SU8010). Valence band characteristics were interrogated via high-resolution monochromatic X-ray photoelectron spectrometry (Kratos AXIS UltraDLD instrumentation, Japan) for quantitative compositional profiling at near-surface domains.

Free chlorine concentrations in the system were determined using the *N,N*-diethyl-*p*-phenylenediamine (DPD) method [33]. Nitrate (NO_3^-) and nitrite (NO_2^-) ions were analyzed using ion chromatography (Dionex, USA), and NH_3 was detected with Nessler reagent via a UV-visible spectrophotometer set to 420 nm [34]. The electrochemical behavior of $\text{RuO}_2@\text{PbO}_2\text{-M}$ was tested using linear sweep voltammetry (LSV). Total nitrogen (TN) removal levels were measured with a multi N/C 3100 TOC/TN analyzer (Analytik Jena, Germany). NB, TBA, and NaHCO_3 were measured using high-performance liquid chromatography (HPLC; LC-20AT, Shimadzu, Japan) with a C18 column. Detection wavelengths were set at 266 nm for NB, 227 nm for TBA, and 230 nm for NaHCO_3 [35].

2.4. Evaluation of denitrification and decarbonization performance of $\text{RuO}_2@\text{PbO}_2\text{-M}$

The denitrification and decarbonization performance of $\text{RuO}_2@\text{PbO}_2\text{-M}$ was evaluated using $(\text{NH}_4)_2\text{SO}_4$ and APAP as model pollutants in a laboratory-scale dead-end filtration setup. A round membrane coupon with an effective area of 17.34 cm^2 was prepared. Next, a terminal filtration tank was used with deionized water passing through for 30 min at a residence time of 1.12 min to achieve a stable permeate flux.

2.5. Determination of the concentration of radical species

NB, TBA, and NaHCO_3 were used as the probes to quantify the steady-state concentrations of $\cdot\text{OH}$, $\cdot\text{Cl}$, and $\cdot\text{ClO}$ in the $\text{RuO}_2@/\text{PbO}_2\text{-M}$ elector-filtration system.

3. Results and Discussion

3.1. Synthesis and characterization of $\text{RuO}_2@/\text{PbO}_2\text{-M}$ nanostructures on Ti-M

Nanostructured PbO_2 and RuO_2 supports was synthesized on Ti-M to enhance the electrocatalytic activity and electrode stability of EM, $\text{PbO}_2\text{-M}$ as illustrated in Fig. 1(a). Next, the RuO_2 supports were seeded onto the as-built $\text{PbO}_2\text{-M}$ scaffold by templating to produce $\text{RuO}_2@/\text{PbO}_2\text{-M}$ (Fig. 1(a)).

The surface morphology and structure of the electrodes were characterized using scanning electron microscopy. The result showed that the surface of the $\text{RuO}_2@/\text{PbO}_2\text{-M}$ gel coating was uniform and dense without discernible boundaries between the PbO_2 grains. EDS mapping was used to evaluate the elemental distribution patterns of the EMs. As illustrated in Fig. 1(b), the functionalization of PbO_2 and RuO_2 resulted in a uniform distribution of Ti (blue) along with Pb (green) and Ru (purple), thereby confirming the effective dispersion of RuO_2 and PbO_2 on the $\text{RuO}_2@/\text{PbO}_2\text{-M}$ composite. The XRD peaks of Ti-M were ascribed only to titanium anatase (JCPDS NO. 73-0851). Fig. 1(c) displays the XRD patterns of $\text{RuO}_2@/\text{PbO}_2\text{-M}$, with diffraction peaks at 25.4° , 36.2° , and 49.0° corresponding to the (1 1 0), (1 0 1), and (2 1 1) planes of the $\beta\text{-PbO}_2$ phase (JCPDS NO. 42-1121), respectively. It has been reported that $\beta\text{-PbO}_2$ is primarily electrodeposited in acidic electrolytes containing fluorides [36]. Furthermore, the presence of a RuO_2 diffraction peak at 53.3° for $\text{RuO}_2@/\text{PbO}_2\text{-M}$ was confirmed by comparison with a reference standard (JCPDS NO. 04-1209).

This series of EMs designs provides a unique research object for studying a relatively constant surface-to-volume ratio (SVR) while significantly altering the cross-sectional dimensions of the EMs flow channels. The preparation of the PbO_2 and RuO_2 functional layers caused a reduction in the pore size of the EMs, which consequently resulted in a decrease in the porosity (Fig. 1(d)). Contrariwise, $\text{RuO}_2@/\text{PbO}_2\text{-M}$ nanocomposites featuring reduced mesoporous dimensions demand substantially augmented hydraulic potential gradients—quantified via the viscous flux dependence principle (Hagen-Poiseuille formalism)—when benchmarked against macroporous Ti-M substrates in isoperistaltic filtration paradigms (Fig. 1(e)).

Fig. 1(f) shows the chemical composition of the $\text{RuO}_2@/\text{PbO}_2\text{-M}$ determined by XPS. Analysis was performed to assess the surface chemical composition and valence states of the $\text{RuO}_2@/\text{PbO}_2\text{-M}$ electrode. The O 1s spectrum exhibited an asymmetric peak, deconvoluted into two components at binding energies of 531.0 and 529.2 eV, corresponding to O–Pb and O–Ru interactions, respectively [37,38]. Characteristic peaks at 137.6 and 142.5 eV were identified for the Pb $4f_{7/2}$ and Pb $4f_{5/2}$ orbitals, which indicates the presence of Pb^{2+} . Additionally, Ru 3d exhibited peaks at 280.6 and 284.8 eV, corresponding to $3d_{5/2}$ and $3d_{3/2}$ of Ru^{4+} . The presence of O–Ru bonds suggests surface oxidation [39], which explains the absence of Ru peaks in the XRD patterns of Ti-M. The synthesis and characterization of $\text{RuO}_2@/\text{PbO}_2\text{-M}$ demonstrated its improved electrocatalytic activity and stability.

3.2. Enhanced electrochemical performance of the $\text{RuO}_2@/\text{PbO}_2\text{-M}$ electrodes

In this study, the electrochemical behavior of the Ti-M, $\text{PbO}_2\text{-M}$, and $\text{RuO}_2@/\text{PbO}_2\text{-M}$ electrodes was investigated using a standard

three-electrode electrochemical cell, as shown in Fig. 2(a). The measured oxygen evolution potentials (OEP) of Ti-M, $\text{PbO}_2\text{-M}$, and $\text{RuO}_2@/\text{PbO}_2\text{-M}$ were 1.64, 1.65, and 1.76 eV, respectively. Notably, the incorporation of Ru significantly enhanced the OEP of the electrodes [40]. Elevated OEPs are beneficial because they inhibit undesired oxygen evolution reactions, facilitate radical formation, and improve electrocatalytic oxidation efficiency, thereby contributing to reduced energy consumption [41].

Fig. 2(b) shows the Nyquist plots for the different electrodes, with detailed simulation results provided in the Table S1 in Appendix A. The inset shows the equivalent-circuit model. Within the constructed equivalent circuit topology, R_s explicitly quantifies bulk electrolytic ohmic dissipation, Q_{dl} and R_{ct} jointly epitomize Helmholtz-plane stored charge density and activation-controlled charge traversal barrier, respectively, while the Q_{ads} and R_{ads} coupling models sorptive phase accumulation dynamics and metastable intermediate species transport impedance at electrochemical interphases, respectively. The analysis reveals that the first high-frequency semicircle is consistently smaller than the second low-frequency semicircle for Ti-M, $\text{PbO}_2\text{-M}$, and $\text{RuO}_2@/\text{PbO}_2\text{-M}$, which indicates that the kinetics of these electrodes are primarily governed by the slower adsorption and desorption processes of intermediates (that is, $R_{ct} \ll R_{ads}$). Furthermore, $\text{PbO}_2\text{-M}$ exhibited a smaller high-frequency semicircle than Ti-M, suggesting that $\text{RuO}_2@/\text{PbO}_2\text{-M}$ exhibited an accelerated charge-transfer rate [42]. A corresponding trend was observed for R_{ads} , whereas Q_{ads} exhibited an inverse relationship. A lower R_{ads} and higher Q_{ads} typically signify the generation of more radicals at the electrode surface, which is advantageous for the electrocatalytic oxidation of pollutants [43]. Furthermore, the pronounced variation in R_{ads} relative to R_{ct} highlights the critical role of RuO_2 modified $\text{PbO}_2\text{-M}$ in regulating the surface structural characteristics. Figs. 2(c) and (d) present the Tafel slopes and electrochemically active surface area (ECSA) curves, respectively, demonstrating that $\text{RuO}_2@/\text{PbO}_2\text{-M}$ possesses a greater number of active sites and enhanced electrocatalytic activity [44].

3.3. Enhanced ammonia oxidation performance of electro-filtration systems using $\text{RuO}_2@/\text{PbO}_2\text{-M}$ anodes

In this study, the ammonia oxidation performances of electro-filtration systems was investigated using various electrode materials: Ti-M, $\text{PbO}_2\text{-M}$, and $\text{RuO}_2@/\text{PbO}_2\text{-M}$. A concentration of $100 \text{ mg}\cdot\text{L}^{-1}$ $(\text{NH}_4)_2\text{SO}_4$ was selected as the simulated pollutant for performance evaluation. Notably, a decrease in the flow rate increased the time spent within the pores, analogous to the extension of the reaction time in a batch reactor.

As illustrated in Fig. 3(a), significant decomposition of $\text{NH}_3\text{-N}$ occurred within a residence time (t_R) of 1 min. Control experiments indicated that Ti-M initially removed only a small portion of $\text{NH}_3\text{-N}$, likely owing to physical adsorption during the electro-filtration process.

Fig. 3(b) shows that the $\text{NH}_3\text{-N}$ degradation kinetics induced by $0.25\text{RuO}_2@/\text{PbO}_2\text{-M}$ were significantly faster than those induced by Ti-M and $\text{PbO}_2\text{-M}$. The rate constant for the probe reaction in the EMs with the largest pore size, Ti-M, was measured at 0.25 s^{-1} (Fig. 3(b)). In contrast, when the RuO_2 concentration was 0.25 wt% (that is, $0.25\text{RuO}_2@/\text{PbO}_2\text{-M}$), the rate constant significantly increased to 2.70 s^{-1} , manifesting an undecimal throughput augmentation factor relative to batch processing kinetics. The half-life (τ_H) of the reaction of the electro-filtration system is inversely proportional to K_{obs} , and decreased from approximately 120 s for Ti-M to 36 s for $\text{PbO}_2\text{-M}$, and down to approximately 14 s for $0.25\text{RuO}_2@/\text{PbO}_2\text{-M}$. Notably, even when these rate constants were normalized using the SVR, the kinetic enhancement remained substantial.

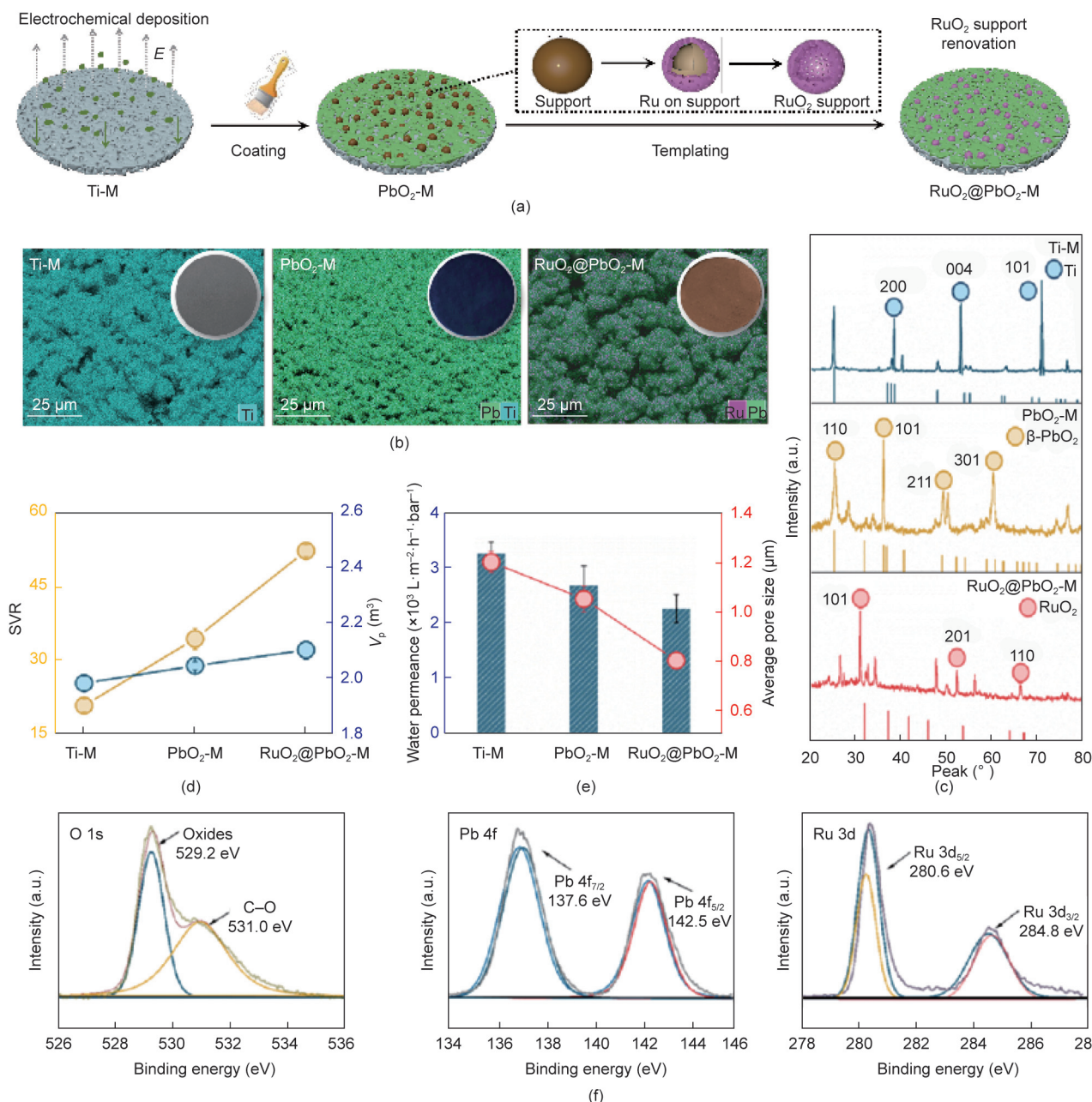


Fig. 1. Fabrication and characterization of the Ti-M, PbO₂-M, and RuO₂@PbO₂-M. (a) Schematics illustrating the fabrication protocol of the PbO₂-M and RuO₂@PbO₂-M. *E*: electric field. (b) SEM images of the Ti-M, PbO₂-M, and RuO₂@PbO₂-M. EDS mapping images of the as-prepared Ti-M, PbO₂-M, and RuO₂@PbO₂-M. Relevant photonic canvases evince monotonic spatial dispersion patterns for Ti-derived signals (blue) element in the Ti-M, Ti and Pb (green) elements in PbO₂-M, and Pb and Ru (purple) elements in the RuO₂@PbO₂-M. The insets show the photos of each membrane coupon. (c) XRD patterns of the Ti-M, PbO₂-M, and RuO₂@PbO₂-M. The Ti (JCPDS NO.73-0851), β -PbO₂ (JCPDS NO.42-1121), and RuO₂ (JCPDS NO.04-1209) phases are used as references for identifying the crystal planes of Ti-M, PbO₂-M, and RuO₂@PbO₂-M. (d) The surface-to-volume ratio (i.e., SVR) and pore volume (V_p , m^3) of the Ti-M, PbO₂-M, and RuO₂@PbO₂-M. (e) The water permeance and average pore sizes of the Ti-M, PbO₂-M, and RuO₂@PbO₂-M. (f) High-resolution XPS spectra of O 1s, Pb 4f, and Ru 3d of the RuO₂@PbO₂-M.

The Sankey diagram in Fig. 3(c) illustrates the mass flow of ammonia oxidation through different EMs, and clearly depicts the conversion pathways of NH₃-N. This is consistent with the results shown in Fig. 3(a), which indicate that 0.25RuO₂@PbO₂-M exhibited both high NH₃-N removal efficiency and effective N₂ selectivity, while producing a lower yield of NO₃⁻-N. Additionally, statistical calculations of energy consumption (EnC) and average current efficiency (ACE) was performed for ammonia removal using composite membranes I–V, including Ti-M, PbO₂-M, 0.2RuO₂@PbO₂-M, 0.25RuO₂@PbO₂-M, and 0.3RuO₂@PbO₂-M. These findings suggest that 0.25RuO₂@PbO₂-M offers significant

advantages as an electro-filtration anode, characterized by a high current efficiency and low energy consumption (Fig. 3(d)).

3.4. Experiment on factors influencing optimization under electro-filtration conditions

This study investigated the impacts of various operational parameters on the nitrogen removal performance of a catalyst 0.25RuO₂@PbO₂-M, utilizing a controlled variable approach. Key parameters examined include current density, pH, chloride ion (Cl⁻) concentration, and initial ammonia concentration. Single

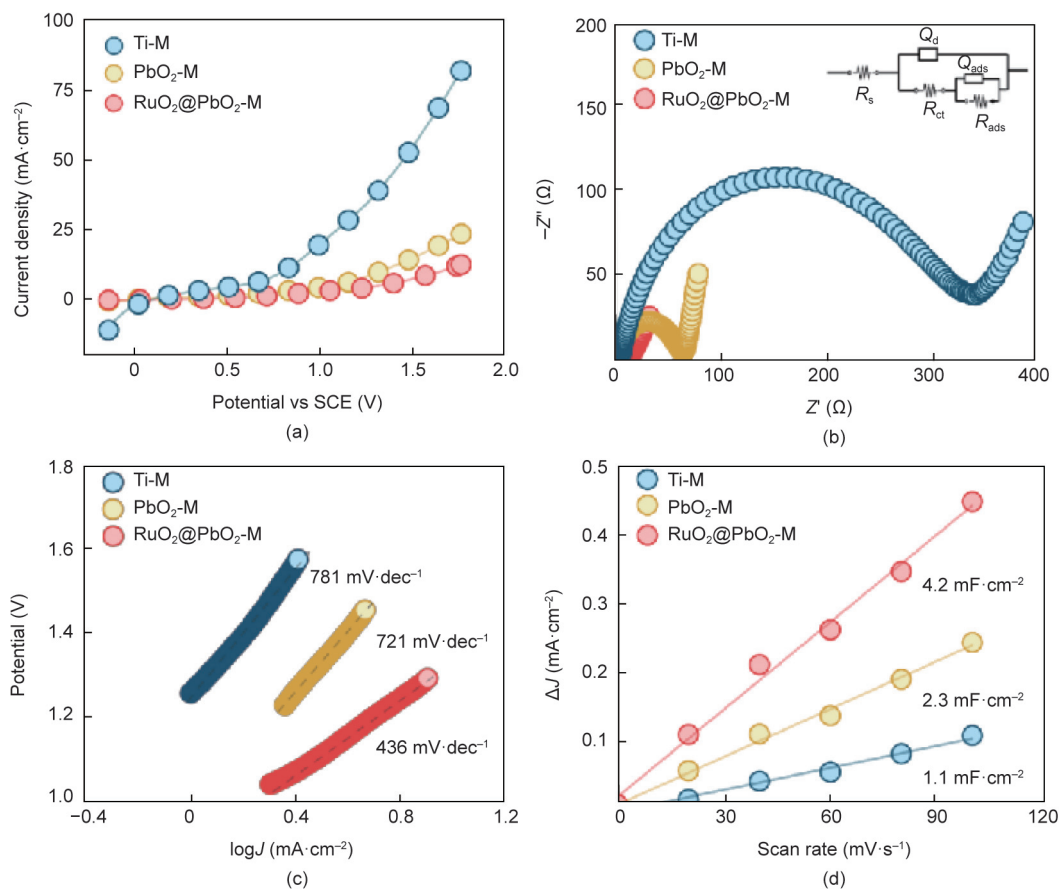


Fig. 2. Electrochemical properties of the Ti-M, PbO₂-M, and RuO₂@PbO₂-M. (a) LSV curves of the Ti-M, PbO₂-M, and RuO₂@PbO₂-M acquired by a potential range of -0.5 to 1.8 V vs saturated calomel electrode (SCE) at a scan rate of 100 mV·s⁻¹ and room temperature. (b) The Nyquist plots and (c) Tafel slope curves of the Ti-M, PbO₂-M, and RuO₂@PbO₂-M applied with alternating current (AC) frequencies varying from 100 kHz to 0.1 Hz in 10 mg·L⁻¹ Na₂SO₄ solution. (d) Double-layer capacitance (C_{dl}) plots of Ti-M, PbO₂-M, and RuO₂@PbO₂-M analyzed upon current–voltage (CV) curves. Unless otherwise noted, the membranes for the above-mentioned measurements were used membrane electrode with an effective working area of 17.34 cm². Z denotes impedance, J denotes current density, dec: decade.

electro-filtration mode was employed with 0.25RuO₂@PbO₂-M to maintain a membrane pore retention time of 1.12 min. Continuous electro-filtration was performed for 1 h to assess the efficiency of ammonia removal under the specified conditions.

As shown in Fig. 4(a), an increase in the current density enhanced the removal of NH₃-N. At higher current densities, more active chlorine, ·Cl, and ·OH were generated, which significantly boosted the removal rate and denitrification efficiency of NH₃-N. Conversely, lower current densities resulted in reduced generation of ·OH and HClO at the electrode surface. However, excessively high current densities can cause intensified side reactions, such as oxygen evolution, which oxidizes ·OH to H₂O and decrease the concentration of ·ClO radicals in the solution. This reduction hampers denitrification [45,46]. Additionally, electro-filtration degradation experiments were performed with initial NH₃-N concentrations ranging from 0 to 300 mg·L⁻¹ (Fig. 4(b)). It was determined that the NH₃-N initial concentration is positively correlated with the degradation rate.

When the chloride ion concentration was 0 mmol·L⁻¹, the solution lacked chloride ions, resulting in a NH₃-N removal rate of only 12.6% within 60 min (Fig. 4(c)). It is believed that ·OH is the primary active species generated by the electrode, which catalytically oxidizes NH₃-N in the solution to NO₃⁻. However, as the chloride ion concentration increased from 50 to 300 mmol·L⁻¹, the removal rate of NH₃-N dramatically increased from 12.6% to 99.7%. This indicated that the presence of chloride ions significantly enhanced

the removal of NH₃-N in the RuO₂@PbO₂-M system. Chloride ions quickly ionize near the anode, producing active chlorine, which facilitates the degradation of NH₃-N because of the rapid increase in the active species. As the amount of active chlorine in the solution increased, the concentrations of OCl⁻ and ·Cl also increased. However, when the concentration reached a certain value, the ·Cl concentration gradually decreased. As ·OH reacts with ·Cl, the concentration of ·Cl decreased while that of ·ClO increased. This is because, in the presence of ·OH, the synergistic oxidation of active oxygen species groups generates ·ClO at a much faster rate than the reaction of ·Cl with active chlorine to form ·ClO. Therefore, the RuO₂@PbO₂-M electrode system exhibited enhanced oxidative activity.

From the changing pattern of the data in Fig. 4(d), it was observed that under acidic conditions, the increased concentration of H⁺ in the solution promoted the reduction of H⁺ to generate hydrogen gas (H₂), thereby accelerating the rates of electron and mass transfer [47]. In contrast, under strongly alkaline conditions, the denitrification efficiency decreased from 96.3% at pH 3 to 3.9% at pH 9. This decline may be attributed to corrosion of the 0.25RuO₂@PbO₂-M electrode surface by the highly alkaline solution, which diminishes the oxidative capability of the electrode. In summary, the optimal operating conditions were a current density of 20 mA·cm⁻², chloride ion concentration of 100 mg·L⁻¹, acidic pH, and retention time of 1.12 min, which resulted in an NH₃-N removal efficiency of approximately 99.7%.

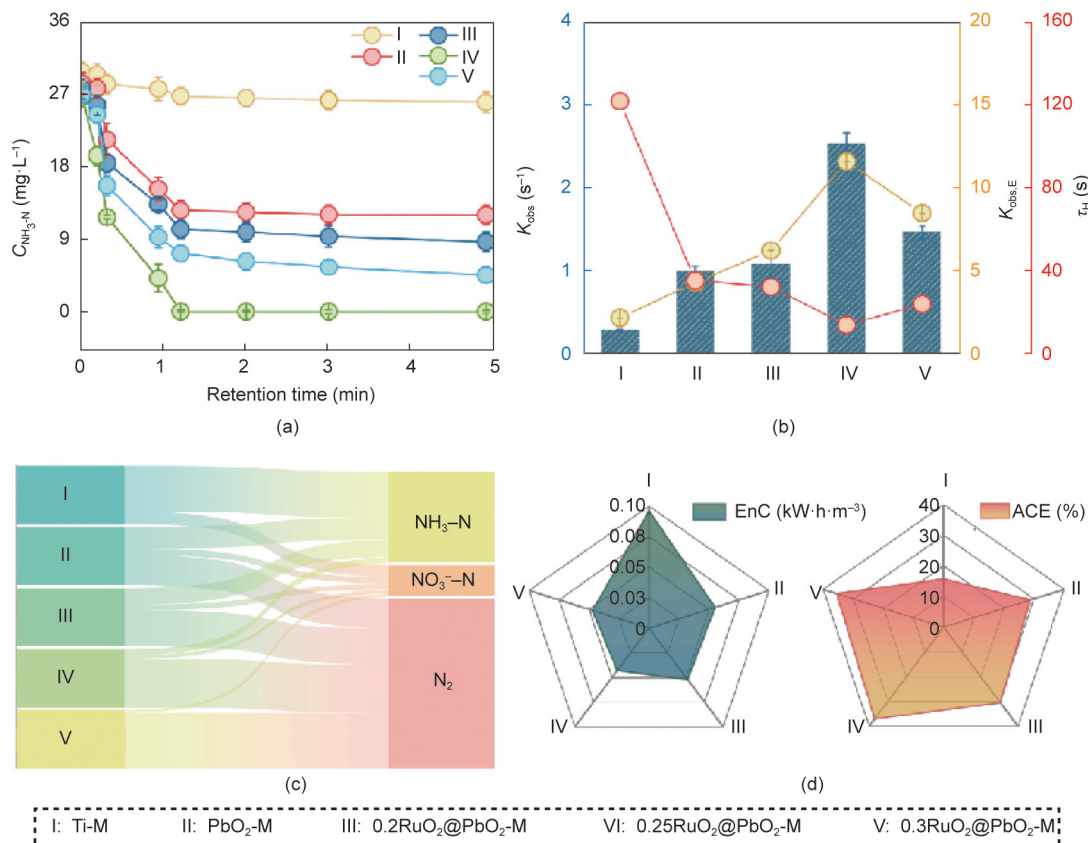


Fig. 3. Ammonia oxidation performance of the electro-filtration using different composite membranes. (a) $\text{NH}_3\text{-N}$ concentration ($C_{\text{NH}_3\text{-N}}$) versus retention time as a function of the Ti-M, PbO₂-M, 0.2RuO₂@PbO₂-M, 0.25RuO₂@PbO₂-M, and 0.3RuO₂@PbO₂-M (membranes I–V). (b) Pseudo-first-order rate constants (K_{obs}) of ammonia oxidation over different membranes (left y-axis) and the rate constant ratio ($K_{\text{obs,E}}$) of the membranes to a general electrochemical batch reactor with normalized SVR (right yellow y-axis). The right red y-axis shows the half-life (τ_{H}) of $\text{NH}_3\text{-N}$ over the membranes I–V. (c) Sankey diagram for the mass flow of ammonia oxidation by electro-filtration. (d) Energy consumption (EnC) and average current efficiency (ACE) of the composite membranes I–V calculated for ammonia removal.

3.5. Role of the reactive radicals in $\text{NH}_3\text{-N}$ removal during electro-filtration

To elucidate the roles of $\cdot\text{OH}$, $\cdot\text{Cl}$, and $\cdot\text{ClO}$ in the effective removal of $\text{NH}_3\text{-N}$ during the electro-filtration process utilizing RuO₂@PbO₂-M, quenching experiments were performed with specific scavengers, as shown in Fig. 5(a). NB, TBA, and NaHCO₃ served as specific scavengers of $\cdot\text{OH}$, $\cdot\text{Cl}$, and $\cdot\text{ClO}$, respectively [48,49]. Notably, the efficient quenching observed with NaHCO₃ underscores the predominant role of $\cdot\text{ClO}$ in $\text{NH}_3\text{-N}$ removal. In contrast, NB only inhibited $\text{NH}_3\text{-N}$ conversion by 23%, indicating that $\cdot\text{OH}$ is not the principal radical facilitating the direct transformation of NH_3 to N_2 .

Furthermore, electron paramagnetic resonance (EPR) spectroscopy was employed using 5,5-dimethyl-1-pyrroline *N*-oxide (DMPO) as a spin-trap reagent to identify the oxidative radicals involved (Fig. 5(b)). Signals corresponding to DMPO- $\cdot\text{OH}$ confirmed the generation of $\cdot\text{OH}$, while DMPO- $\cdot\text{ClO}$ signal and additional low-intensity peaks suggested the presence of $\cdot\text{Cl}$ [50]. The intensities of $\cdot\text{OH}$ and $\cdot\text{ClO}$ signals in 0.25 RuO₂@PbO₂-M system were significantly higher than those in the PbO₂-M system, which indicates the crucial role of $\cdot\text{ClO}$ radical-driven oxidation in RuO₂@PbO₂-M. To further investigate the involvement of $\cdot\text{OH}$ in $\cdot\text{ClO}$ generation, the degradation of $\text{NH}_3\text{-N}$ by HClO in the presence and absence of the PbO₂-M photoanode was compared. The results demonstrated a significant increase in degradation rates when PbO₂-M was employed, suggesting that HClO is converted to the more reactive $\cdot\text{ClO}$.

As illustrated in Fig. 5(c), the oxidation degradation of $\text{NH}_3\text{-N}$ at the RuO₂@PbO₂-M electrode inhibited chlorite oxidation, thereby reducing the active chlorine consumption. Consequently, the concentration of active chlorine rises over time, which enhances $\cdot\text{ClO}$ generation. The spatial distribution of $\cdot\text{OH}$ indicates that elevated $\cdot\text{OH}$ concentrations are advantageous for pollutant degradation. Under indirect oxidation conditions with added chloride ions, RuO₂@PbO₂-M electrodes facilitate the rapid reaction between ClO^- with $\cdot\text{OH}$ and $\cdot\text{Cl}$, which promotes the formation $\cdot\text{ClO}$ radicals. However, as $\cdot\text{ClO}$ generation increases, a portion is subsequently consumed.

3.6. Simultaneous denitrification and decarbonization of amino-containing pollutants in an electrified flow-through membrane system

APAP was selected as the model for assessing the simultaneous denitrification and decarbonization capabilities of RuO₂@PbO₂-M through *in situ* $\cdot\text{ClO}$ generation within an electrified flow-through membrane filtration system, as illustrated in Fig. 6(a). Manifests 1.12-minute void-phase confinement duration per unidirectional cycle, volumetrically mapped through orthogonal permeation vector partitioning in membranous tortuosity domains. The interwoven architecture of RuO₂@PbO₂-M, synthesized using a templating method, effectively immobilized the Ru and Pb catalysts within the Ti-M framework. This design promoted the simultaneous exposure of active sites while maintaining the structural integrity and conductivity (Fig. 6(b), left). This unique configuration enhances the oxidative activity towards $\text{NH}_3\text{-N}$ and chemical oxygen

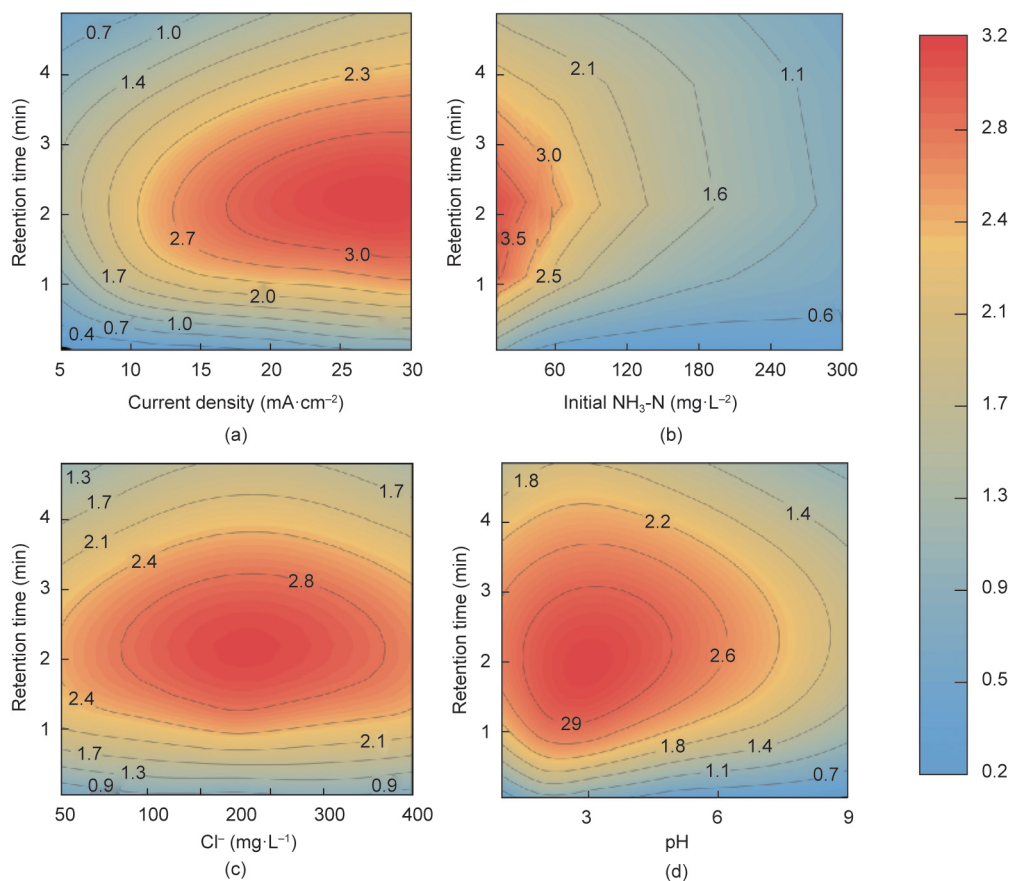


Fig. 4. Influencing factors for ammonia removal. Retention time response of electro-filtration and (a) current density, (b) initial concentration of NH₃-N, (c) Cl⁻ concentration, and (d) pH to pseudo-first-order rate constants of NH₃-N removal. Kriging interpolation was used to generate the contour plots.

demand (COD) during the electro-filtration process, leveraging convection-enhanced mass transfer. The convective movement of water through the EMs reduces the diffusion boundary layer to a scale comparable to the pore radius, which significantly improves both the mass transport rates and the Faradaic efficiency of electrocatalytic oxidation. Fig. 6(b), right illustrates two key steps in simultaneous denitrification and decarbonization, highlighting that ·ClO formation serves as the rate-determining step (orange box). The proposed pathway for concurrent nitrogen and carbon removal is depicted in the gray box in Fig. 6(b). Ruthenium is widely recognized for its catalytic efficacy in the electrochemical reduction of NH₃ to N₂ because of its high activity in the initial charge-transfer step of the rate-determining reaction; however, it does not mineralize organic pollutants. This study demonstrates the structural advantages and feasibility of achieving efficient selective oxidation along with simultaneous nitrogen and carbon removal by circulating electro-filtration under chlorination conditions.

The efficacy of RuO₂@PbO₂-M for the removal of four prevalent amine contaminants, lysine (LYS), anamorelin (ANI), APAP, and tetracycline (TC), from industrial and pharmaceutical wastewater was investigated (Fig. 6(c)). APAP, a widely used antipyretic and analgesic, is an emerging phenolic pollutant in aquatic environments that poses significant risks to liver, metabolic, and neurological health upon human exposure [51]. Organic pollutants containing amino groups with different carbon-to-nitrogen (C/N) ratios was selected. Notably, the ammonia-nitrogen removal rate decreased as the C/N ratio increased, which highlights the complex interactions in the treatment process. ·OH exhibited a preferential reactivity towards organic carbon over denitrification, with C–C single bonds degrading more readily than benzene rings, thereby

rendering polycyclic organic pollutants more susceptible to degradation. Specifically, the removal rate of NH₃-N from total carbon was 20%, whereas the COD removal efficiency reached 80%. This indicates that ·ClO primarily targets carbon during simultaneous denitrification and decarbonization, with reactive species subsequently engaging NH₃-N, contingent on sufficient ·ClO concentrations.

Five comparative experiments were performed to evaluate the NH₃-N oxidation and APAP removal efficiencies of different EMs under controlled conditions. As shown in Fig. 6(d), a clear relationship exists between the EMs and the residual NH₃-N concentrations in the permeate after 1 h. Notably, at the RuO₂ doping ratio of 0.25 wt%, the selectivity for N₂ increased (Fig. 6(d), right). The removal efficiencies for APAP was ranked as follows: 0.25RuO₂@PbO₂-M > 0.3RuO₂@PbO₂-M > 0.2RuO₂@PbO₂-M > PbO₂-M > Ti-M. These variations reflect the distinct reactive species produced by each EMs, with the synergistic effects of oxidizing agents, such as ·OH and ·Cl, playing a crucial role in NH₃-N removal. In electro-filtration systems dominated by ·OH, the concurrent presence of ammonia nitrogen and organic compounds favors the oxidation of the latter, inhibiting NH₃-N removal. Conversely, in the presence of chloride ions, ·Cl effectively targets the nitrogen atoms of NH₃-N, enhancing its removal through chlorine-mediated reactions [51].

Liquid chromatography-mass spectrometry (LC-MS; Waters e2695, Walters, USA) was employed to identify the intermediates formed during APAP degradation and elucidate the potential degradation pathways. NaCl served as the electrolyte, and ·OH were identified as the primary active species. Theoretical calculations indicated that the carbon sites on the aromatic ring, particularly C6 and C9, as well as the N4 position, exhibit significant

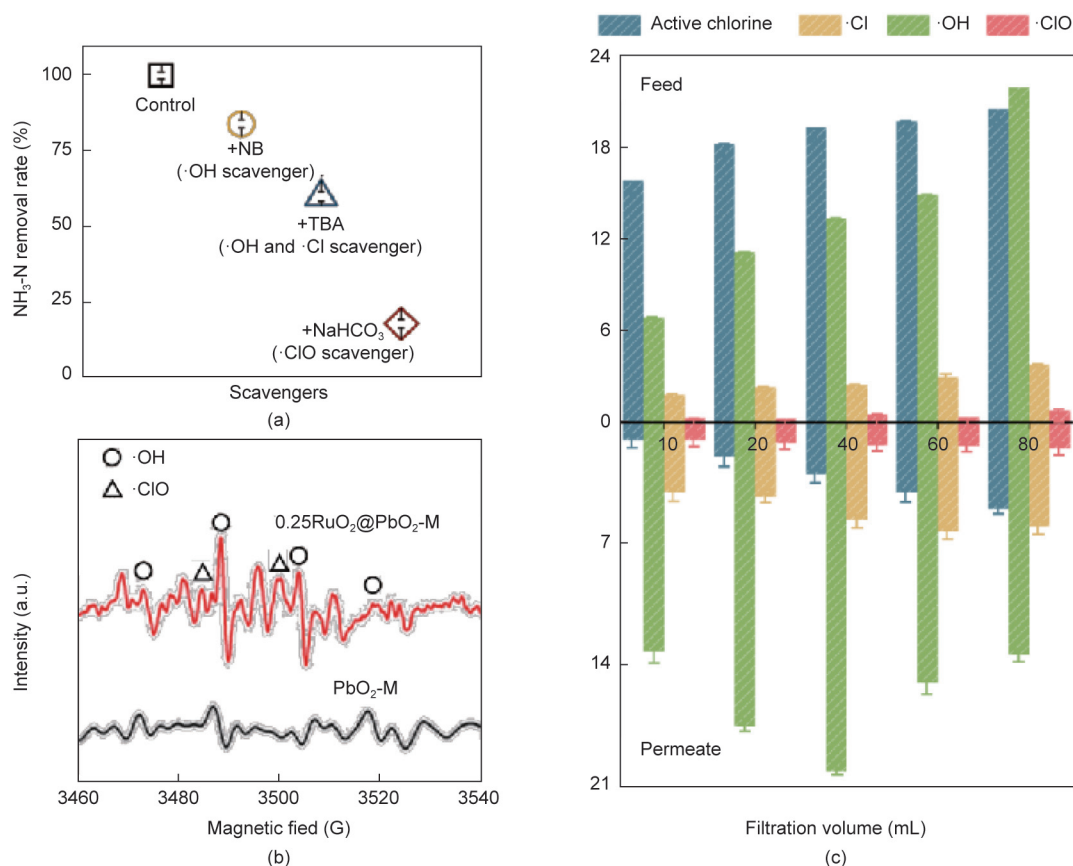


Fig. 5. Spatiotemporal distribution of the active species generated in the electro-filtration system using $\text{RuO}_2@\text{PbO}_2\text{-M}$. (a) Removal rates of $\text{NH}_3\text{-N}$ in $\text{RuO}_2@\text{PbO}_2\text{-M}$ electro-filtration system with the addition of different scavengers such as NB, TBA, and NaHCO_3 . (b) ESR spectra of the permeates of the $\text{PbO}_2\text{-M}$ and $\text{RuO}_2@\text{PbO}_2\text{-M}$ electro-filtration systems with the addition of DMPO in the feed. (c) Spatial and temporal distribution of the free radicals OH, Cl, and ClO, and active chlorine in the feed and permeate of the electro-filtration system.

susceptibility to attack by reactive species (Fig. S1 in Appendix A). APAP mineralization initiates via radical addition trajectories targeting the biphenylic linkage (C5–C10) or heterocyclic N4 nucleus, precipitating three divergent pathways: peri-carbon oxygenation at electrophilic loci (C5/C10), azotic center nucleophilic displacement, and acetyl fission as corroborated computationally (Fig. S1). These initial reactions yield various intermediates, including p-aminophenol and hydroquinone, as well as their hydroxylated derivatives. This degradation profile aligns with the findings of other advanced oxidation processes (AOPs). The intermediates identified by LC-MS analysis (M1–M11) are listed in Table S2 in Appendix A. The proposed degradation pathways are shown in Fig. 6(e).

An intermediate with a mass-to-charge ratio (m/z) of 300 was also identified, which was hypothesized to be an APAP dimer (M2) [52]. This dimer may undergo transformations such as deacetylation, hydroxylation, and hydroxyl substitution, resulting in products M4 through M5. Alternatively, degradation may occur through ring-opening reactions, yielding simpler intermediates characterized by a single aromatic structure (e.g., M6). Ultimately, these intermediates may be further oxidized into low-molecular-weight organic compounds (e.g., M9) and completely mineralized CO_2 , H_2O , and inorganic nitrogenous ions (NH_3 and NO_3^-). Alternatively, M6 can yield M7 and M10 through chlorination and oxidation reactions, during which ammonia is oxidized to N_2 [53]. AOPs and EAOR are recognized as effective technologies for converting bio-refractory organic compounds, such as APAP, into benign inorganic end products.

3.7. Advanced electro-filtration system for high-concentration ammonia nitrogen wastewater treatment.

Fig. 7 illustrates the treatment process for high-concentration $\text{NH}_3\text{-N}$ wastewater. In this system, industrial raw water is introduced into an electro-filtration unit through mixing and primary settling tanks, utilizing pumps for efficient transfer. The tertiary electro-filtration system employs a coupling of point addition and filtration to ensure that the treated effluent meets established quality standards prior to discharge. The effluent was categorized into three stages: 1st, 2nd, and 3rd. After 36 h of continuous operation, $\text{RuO}_2@\text{PbO}_2\text{-M}$ demonstrated low energy consumption and high current density (Fig. 7(e)), with an average EnC value of approximately $0.06 \text{ kWh}\cdot\text{m}^{-3}$, corresponding to an operational cost of approximately $0.00435 \text{ CNY}\cdot\text{t}^{-1}$, which results in significantly reduced operational costs compared to the current benchmarks, both domestically and internationally. Metal-ion leaching experiments performed at various filtration stages (Fig. 7(c)) indicated that increased impact forces enhanced water flow across the membrane, which caused elevated Pb^{2+} leaching from the electrode material. However, the system stability over time correlated with a reduction in metal leaching. After 84 h of operation, the COD of the effluent decreased from 1570 to $225 \text{ mg}\cdot\text{L}^{-1}$, while the ammonia nitrogen concentrations reduced from 503.50 to $4.84 \text{ mg}\cdot\text{L}^{-1}$ through secondary electro-filtration, both achieving composite discharge standards. In summary, the system effectively reduced $\text{NH}_3\text{-N}$ and COD, ensuring efficient compliance with the discharge standards.

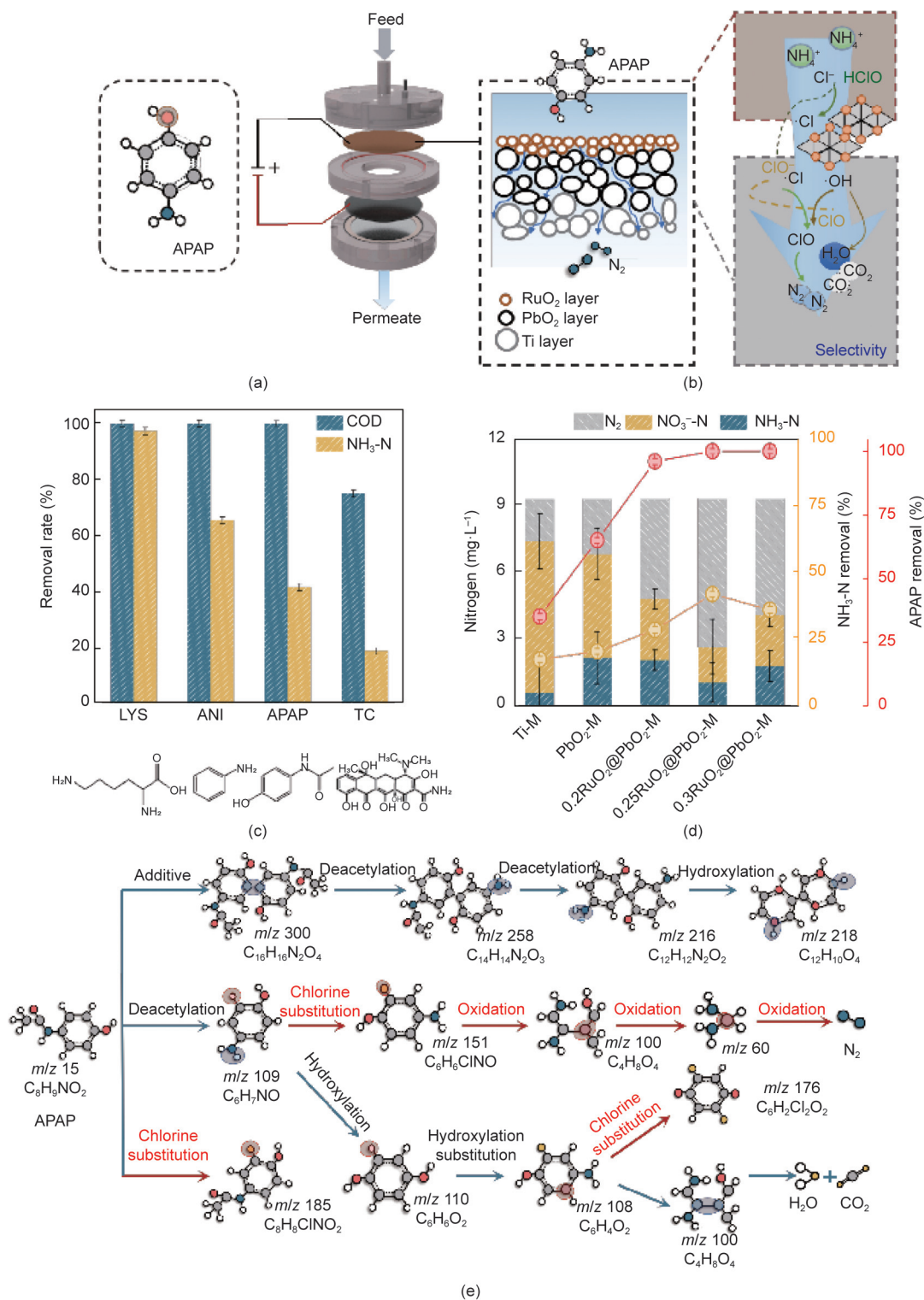


Fig. 6. Simultaneous denitrification and decarbonization of simulated wastewater using the RuO₂@PbO₂-M electro-filtration membrane reactor. (a) Schematic illustration of the electro-filtration system containing a RuO₂@PbO₂-M (brown membrane) and an electro-filtration module with a feed chamber, permeate chamber, and the Ti-M (black) for treating APAP-laden simulated wastewater. (b) Schematic diagram of the decomposition of APAP through the RuO₂@PbO₂-M and the generation of active species over the electro-filtration process. The brown, black, and grey realms represent the RuO₂, PbO₂-M, and Ti-M layers, respectively. The green and yellow arrows represent pathways and critical species to actuate denitrification and decarbonization of contaminants. In the anodic region of the electro-filtration, the Cl⁻ and ·OH are generated through electro-filtration methods in close vicinity to the RuO₂@PbO₂-M, attacking the N-center and C–C bond of APAP and generating N₂, H₂O, and CO₂ in the permeate. (c) Removal of four typical amine contaminants through the RuO₂@PbO₂-M electro-filtration process. (d) The concentration of nitrogen (y-axis, black), removal of NH₃-N (y-axis, yellow), and APAP (y-axis, red) in the permeate after the electro-filtration process using different membranes. The electro-filtration processes were performed at current density of 30 mA·cm⁻² and with a retention time of 1.12 min. (e) Proposed denitrification and decarbonization pathway of APAP by electro-filtration.

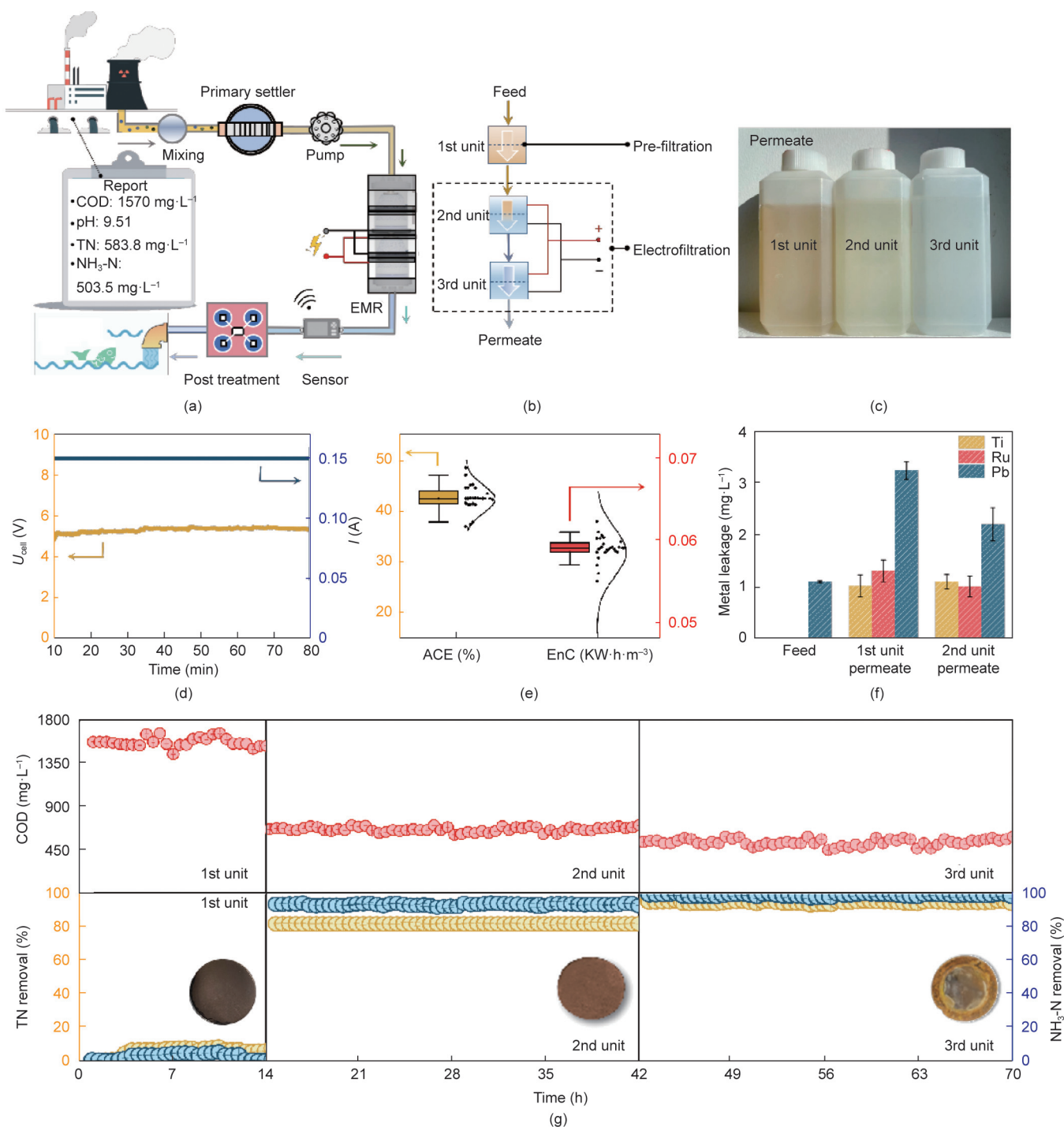


Fig. 7. Simultaneous removal of NH₃-N and COD of a practical wastewater using the RuO₂@PbO₂-M electro-filtration system. (a) Illustration of a typical electrochemical membrane reactor (EMR) system for simultaneous denitrification and decarbonization of a practical hypersaline wastewater containing 503.5 mg·L⁻¹ ammonia. Arrows indicate the direction of water flow. (b) Schematics of the RuO₂@PbO₂-M electro-filtration membrane reactor system. The system includes the pre-filtration (1st unit) and electro-filtration (2nd and 3rd units) processes. (c) Photographs of the permeate of different units. (d) Applied voltage (left y-axis) and current (right y-axis) of the electro-filtration system for treating the practical wastewater. (e) EnC and ACE of the electro-filtration system. (f) Metal leaching in the first and second units of the membrane reactor. (g) COD of the permeate of the three electro-filtration stages (top layer left y-axis). TN concentration (bottom layer left y-axis) and NH₃-N removal rates (bottom layer right y-axis) of the permeate of the three electro-filtration stages. The inset shows the photos of the RuO₂@PbO₂-M used in the three units of the membrane reactor. U_{cell} was used to denote the cell voltage, and I was used to represent the current.

4. Conclusions

This study presents the synthesis of RuO₂@PbO₂-M, a novel electrocatalyst that facilitates the ultra-efficient production of ·ClO, thereby significantly enhancing Faradic efficiency and electro-

catalytic performance compared to traditional materials. The simultaneous processes of denitrification and decarbonization was investigated using a single-pass electro-filtration system to elucidate both the feasibility and underlying mechanisms of these processes. The experimental results demonstrated that with a

retention time of merely 1.2 min, the removal rates for $\text{NH}_3\text{-N}$ reached 100%. Furthermore, treating actual high-ammonia wastewater yielded a COD removal rate of 68% and a TN removal rate of 99.6% over a continuous 70 h operational period. The role of ClO in ammonia removal was also investigated, which provided critical insights that could guide future research on electrocatalytic oxidation methodologies. The implications of this research are significant because it proposes a holistic approach to wastewater management that effectively targets ammonia and organic carbon pollutants. This study advances the field of sustainable water treatment technologies and highlights the potential of our electro-filtration system to contribute significantly to environmental engineering practices.

CRedit authorship contribution statement

Bin Zhao: Writing – original draft, Investigation, Formal analysis, Data curation. **Jialin Yang:** Writing – original draft, Formal analysis, Data curation. **Ruiping Liu:** Validation, Supervision, Funding acquisition. **Jiuhui Qu:** Validation, Supervision. **Meng Sun:** Validation, Supervision, Investigation, Funding acquisition, Conceptualization, Writing – review & editing, Writing – original draft.

Declaration of competing interest

The authors declare that they have no known competing financial interests or personal relationships that could have appeared to influence the work reported in this paper.

Acknowledgments

This work was supported by the National Natural Science Foundation of China (52270043), the National Key Research and Development Program of China (2023YFE0113800 and 2024YFC3715000), and the Natural Science Foundation of Beijing Municipality (8242030).

Appendix A. Supplementary data

Supplementary data to this article can be found online at <https://doi.org/10.1016/j.eng.2025.07.016>.

References

- Liu T, Duan H, Lücker S, Zheng M, Daims H, Yuan Z, et al. Sustainable wastewater management through nitrogen-cycling microorganisms. *Nat Water* 2024;2:936–52.
- Zheng M, Hu Z, Liu T, Sperandio M, Volcke EI, Wang Z, et al. Pathways to advanced resource recovery from sewage. *Nat Sus* 2024;7:1394–404.
- Aka RJN, Wu S, Mohotti D, Bashir MA, Nasir A. Evaluation of a liquid-phase plasma discharge process for ammonia oxidation in wastewater: process optimization and kinetic modeling. *Water Res* 2022;224:119107.
- Liao K, You J, Han C, Cheng H, Ren H, Hu H. Dissolved organic nitrogen depresses the expected outcome of wastewater treatment upgrading on effluent eutrophication potential mitigation: molecular mechanistic insight. *Water Res* 2024;122535.
- Hu H, Ren H. Removal of bioavailable dissolved organic nitrogen in wastewater by membrane bioreactors as posttreatment: implications for eutrophication control. *Bioresour Technol* 2019;271:496.
- Zhang X, Sabo R, Rosa L, Niazi H, Kyle P, Byun JS, et al. Nitrogen management during decarbonization. *Nat Rev Earth Environ* 2024;5:717–31.
- Du WJ, Lu JY, Hu YR, Xiao J, Yang C, Wu J, et al. Spatiotemporal pattern of greenhouse gas emissions in China's wastewater sector and pathways towards carbon neutrality. *Nat Water* 2023;1(2):166.
- Chen FY, Wu ZY, Gupta S, Rivera J, Lamberts SV, Pecaut S, et al. Efficient conversion of low-concentration nitrate sources into ammonia on a Ru-dispersed Cu nanowire electrocatalyst. *Nat Nanotechnol* 2022;17(7):759.
- Simon P, Gogotsi Y. Perspectives for electrochemical capacitors and related devices. *Nat Mater* 2020;19(11):1151.
- Chaplin BP. The prospect of electrochemical technologies advancing worldwide water treatment. *Acc Chem Res* 2019;52(3):596.
- Lee SA, Lee MG, Jang HW. Catalysts for electrochemical ammonia oxidation: trend, challenge, and promise. *Sci China Mater* 2022;65(12):3334.
- Du HL, Chatti M, Hodgetts RY, Cherepanov PV, Nguyen CK, Matuszek K, et al. Electroreduction of nitrogen with almost 100% current-to-ammonia efficiency. *Nature* 2022;609(7928):722.
- Xu B, Chen Z, Zhang G, Wang Y. On-demand atomic hydrogen provision by exposing electron-rich cobalt sites in an open-framework structure toward superior electrocatalytic nitrate conversion to dinitrogen. *Environ Sci Technol* 2021;56(1):614.
- Dozzi MV, Brocato S, Marra G, Tozzola G, Meda L, Selli E. Aqueous ammonia abatement on Pt- and Ru-modified TiO_2 : selectivity effects of the metal nanoparticles deposition method. *Catal Today* 2017;287:148.
- Chen C, Li K, Li C, Sun T, Jia J. Combination of Pd–Cu catalysis and electrolytic H_2 evolution for selective nitrate reduction using protonated polypyrrole as a cathode. *Environ Sci Technol* 2019;53(23):13868.
- Gao J, Jiang B, Ni C, Qi Y, Bi X. Enhanced reduction of nitrate by noble metal-free electrocatalysis on P doped three-dimensional Co_3O_4 cathode: mechanism exploration from both experimental and DFT studies. *Chem Eng J* 2020;382:123034.
- Zhou Y, Zhang G, Ji Q, Zhang W, Zhang J, Liu H, et al. Enhanced stabilization and effective utilization of atomic hydrogen on Pd–In nanoparticles in a flow-through electrode. *Environ Sci Technol* 2019;53(19):11383.
- Zhang Y, Li J, Bai J, Li L, Chen S, Zhou T, et al. Extremely efficient decomposition of ammonia N to N_2 using ClO^* from reactions of HO^* and HOCl generated *in situ* on a novel bifacial photoelectroanode. *Environ Sci Technol* 2019;53(12):6945.
- Yuan J, Li Y, Chen X, Yi Q, Wang Z. One electron oxidation-induced degradation of brominated flame retardants in electroactive membrane filtration system: vital role of dichlorine radical-mediated process. *J Hazard Mater* 2024;471:134318.
- Itabashi Y, Asahara H, Ohkubo K. Chlorine-radical-mediated C–H oxygenation reaction under light irradiation. *Chem Commun* 2023;59(49):7506.
- Sun P, Lee WN, Zhang R, Huang CH. Degradation of deet and caffeine under UV/chlorine and simulated sunlight/chlorine conditions. *Environ Sci Technol* 2016;50(24):13265.
- Chuang YH, Chen S, Chinn CJ, Mitch WA. Comparing the UV/monochloramine and UV/free chlorine advanced oxidation processes (AOPs) to the UV/hydrogen peroxide AOP under scenarios relevant to potable reuse. *Environ Sci Technol* 2017;51(23):13859.
- Zhang G, Li B, Shi Y, Zhou Q, Fu WJ, Zhou G, et al. Ammonia recovery from nitrate-rich wastewater using a membrane-free electrochemical system. *Nat Sustain* 2024;7:1251–63.
- Zhao R, Li L, Wu Q, Luo W, Zhang Q, Cui C. Spontaneous formation of reactive redox radical species at the interface of gas diffusion electrode. *Nat Commun* 2024;15(1):8367.
- Shen L, Yu X, Li M, Deng S, Cao H. The *in-situ* generation of ClO^* by single- and dual-atom catalysis of chloride ions to degrade sulfonamide antibiotics: a DFT study. *Chem Eng J* 2024;485:149719.
- Kuang W, Yan Z, Chen J, Ling X, Zheng W, Huang W, et al. A bipolar membrane-integrated electrochlorination process for highly efficient ammonium removal in mature landfill leachate: the importance of ClO^* generation. *Environ Sci Technol* 2022;57(47):18538.
- Shi L, Yin Y, Wang S, Xu X, Wu H, Zhang J, et al. Rigorous and reliable operations for electrocatalytic nitrogen reduction. *Appl Catal B Environ* 2020;278:119325.
- Pei S, Wang Y, You S, Li Z, Ren N. Electrochemical removal of chlorophenol pollutants by reactive electrode membranes: scale-up strategy for engineered applications. *Engineering* 2022;9:77.
- Zhang Y, Zhang T, Huang Z, Yang J. A new class of electronic devices based on flexible porous substrates. *Adv Sci* 2022;9(7):2105084.
- Ji Y, Sun H, Wang X, Yang T, Xue Z, Li C, et al. Vacuum-assisted continuous flow electroless plating approach for high performance Pd membrane deposition on ceramic hollow fiber lumen. *J Membr Sci* 2022;645:120207.
- Wang X, Sun M, Zhao Y, Wang C, Ma W, Wong MS, et al. *In situ* electrochemical generation of reactive chlorine species for efficient ultrafiltration membrane self-cleaning. *Environ Sci Technol* 2020;54(11):6997.
- Zhao Y, Sun M, Wang X, Wang C, Lu D, Ma W, et al. Janus electrocatalytic flow-through membrane enables highly selective singlet oxygen production. *Nat Commun* 2020;11(1):6228.
- Sheng D, Bu L, Zhu S, Wu Y, Wang J, Zhou S. Organic chloramines formation from algal organic matters: insights from Fourier transform-ion cyclotron resonance mass spectrometry. *Water Res* 2021;206:117746.
- Zhang B, Dai Z, Chen Y, Cheng M, Zhang H, Feng P, et al. Defect-induced triple synergistic modulation in copper for superior electrochemical ammonia production across broad nitrate concentrations. *Nat Commun* 2024;15(1):2816.
- Kong X, Wu Z, Ren Z, Guo K, Hou S, Hua Z, et al. Degradation of lipid regulators by the UV/chlorine process: radical mechanisms, chlorine oxide radical (ClO^*)-mediated transformation pathways and toxicity changes. *Water Res* 2018;137:242.
- Ansari A, Nematollahi D. A comprehensive study on the electrocatalytic degradation, electrochemical behavior and degradation mechanism of

- malachite green using electrodeposited nanostructured β - PbO_2 electrodes. *Water Res* 2018;144:462.
- [37] Asbani B, Robert K, Roussel P, Brousse T, Lethien C. Asymmetric micro-supercapacitors based on electrodeposited RuO_2 and sputtered VN films. *Energy Stor Mater* 2021;37:207.
- [38] Wang X, Wang J, Jiang W, Chen C, Wei J, Yu B, et al. MnCo_2O_4 decorating porous PbO_2 composite with enhanced activity and durability for acidic water oxidation. *Fuel* 2023;338:127344.
- [39] Li G, Jang H, Liu S, Li Z, Kim MG, Qin Q, et al. The synergistic effect of Hf–O–Ru bonds and oxygen vacancies in Ru/HfO₂ for enhanced hydrogen evolution. *Nat Commun* 2022;13(1):1270.
- [40] Liu Y, Liang X, Gu L, Zhang Y, Li GD, Zou X, et al. Corrosion engineering towards efficient oxygen evolution electrodes with stable catalytic activity for over 6000 hours. *Nat Commun* 2018;9(1):2609.
- [41] Wei C, Sun S, Mandler D, Wang X, Qiao SZ, Xu ZJ. Approaches for measuring the surface areas of metal oxide electrocatalysts for determining their intrinsic electrocatalytic activity. *Chem Soc Rev* 2019;48(9):2518.
- [42] Li X, Xu H, Yan W. Fabrication and characterization of PbO_2 electrode modified with polyvinylidene fluoride (PVDF). *Appl Surf Sci* 2016;389:278.
- [43] Wang L, Peng M, Chen J, Tang X, Li L, Hu T, et al. High energy and power zinc ion capacitors: a dual-ion adsorption and reversible chemical adsorption coupling mechanism. *ACS Nano* 2022;16(2):2877.
- [44] Anantharaj S, Noda S, Driess M, Menezes PW. The pitfalls of using potentiodynamic polarization curves for tafel analysis in electrocatalytic water splitting. *ACS Energy Lett* 2021;6(4):1607.
- [45] Wu Z, Guo K, Fang J, Yang X, Xiao H, Hou S, et al. Factors affecting the roles of reactive species in the degradation of micropollutants by the UV/chlorine process. *Water Res* 2017;126:351.
- [46] Guo K, Wu Z, Shang C, Yao B, Hou S, Yang X, et al. Radical chemistry and structural relationships of PPCP degradation by UV/chlorine treatment in simulated drinking water. *Environ Sci Technol* 2017;51(18):10431.
- [47] Liu T, Guo M, Orthaber A, Lomoth R, Lundberg M, Ott S, et al. Accelerating proton-coupled electron transfer of metal hydrides in catalyst model reactions. *Nat Chem* 2018;10(8):881.
- [48] Li T, Jiang Y, An X, Liu H, Hu C, Qu J. Transformation of humic acid and halogenated byproduct formation in UV-chlorine processes. *Water Res* 2016;102:421.
- [49] Zhang D, Wang J, Chen H, Gong C, Xing D, Liu Z, et al. Fast hydroxyl radical generation at the air–water interface of aerosols mediated by water-soluble $\text{PM}_{2.5}$ under ultraviolet a radiation. *J Am Chem Soc* 2023;145(11):6462.
- [50] Zhang Y, Li J, Bai J, Shen Z, Li L, Xia L, et al. Exhaustive conversion of inorganic nitrogen to nitrogen gas based on a photoelectron-chlorine cycle reaction and a highly selective nitrogen gas generation cathode. *Environ Sci Technol* 2018;52(3):1413.
- [51] Jiang M, Lu J, Ji Y, Kong D. Bicarbonate-activated persulfate oxidation of acetaminophen. *Water Res* 2017;116:324.
- [52] Liang C, Lan Z, Zhang X, Liu Y. Mechanism for the primary transformation of acetaminophen in a soil/water system. *Water Res* 2016;98:215.
- [53] Li W, Zhang X, Han J. Formation of larger molecular weight disinfection byproducts from acetaminophen in chlorine disinfection. *Environ Sci Technol* 2022;56(23):16929.